Journal of Science and Technology in Civil Engineering, NUCE 2021. 15 (2): 51–66

AN ISOGEOMETRIC FORMULATION WITH A THREE-VARIABLE HIGH ORDER SHEAR DEFORMATION THEORY FOR FREE VIBRATION ANALYSIS OF FG POROUS PLATES REINFORCED BY GRAPHENE PLATELETS

Lieu B. Nguyen[a,*], Thi Bui Viet[b], Hong-Yen Nguyen[c]

[a]*Faculty of Civil Engineering, Ho Chi Minh City University of Technology and Education, 01 Vo Van Ngan street, Thu Duc city, Ho Chi Minh city, Vietnam*
[b]*Center of Construction Inspection and Consulting, CCIC, Thu Dau Mot University, 6 Tran Van On street, Thu Dau Mot city, Binh Duong province, Vietnam*
[c]*Board of Directors Office, Binh Duong University, 504 Binh Duong avenue, Thu Dau Mot city, Binh Duong province, Vietnam*

Article history:
Received 23/12/2020, Revised 31/3/2021, Accepted 01/4/2021

Abstract

We present a generalized three-variable high order shear deformation theory (THSDT) using isogeometric analysis (IGA) to analyze free vibration of functionally graded porous (FGP) plates reinforced by graphene platelets (GPLs) in this work. It is named as FGP-GPLs for a short. The proposed theory only has got three degrees of freedom (DOFs) per node as the same way of numerically solutions in three-dimensional (3D) solids. THSDT fulfills the classical plate theory (CPT), the first-order shear deformation theory (FSDT) and even the higher-order shear deformation theory (HSDT). IGA is chosen to analyze because of its noteworthy advantages in numerical computational sides of plate problems. In addition, the displacement field of THSDT needs the high continuity in approximated formulation with high-order derivatives for a weak form of fourth order equation. According to IGA formulation based on the generalized THSDT, the shear locking phenomenon is free. The variables of THSDT are less than HSDTs which contain five DOFs per node. The influences of weight fractions, the coefficient porosity, dispersion patterns of GPLs and distribution types of porosity on structure's natural frequencies are studied through some numerical examples. In order to prove the reliability and accuracy of present method, the numerical results are compared to available published works.

Keywords: FG-porous plate; graphene platelet reinforcements; three-variable high order shear deformation theory (THSDT); isogeometric analysis; free vibration.

https://doi.org/10.31814/stce.nuce2021-15(2)-05

1. Introduction

The materials with internal holes whose excellent properties such as lightweight, low density, outstanding energy absorbent, heat resistance have been widely used in various fields of engineering [1–5]. In spite of having tremendous properties, the porous materials cause the structural stiffness to

*Corresponding author. *E-mail address:* lieuntb@hcmute.edu.vn (Nguyen, L. B.)

reduce significantly [6]. In order to overpower this shortcoming, the people usually add one in two types of reinforcement such as carbon nanotubes (CNTs) [7–9] and graphene platelets (GPLs) [10, 11] into the porous materials to increase their mechanical properties.

In research field, the porous materials reinforced by GPLs [12] have been received much consideration by the researchers because of their common application in different engineering structures such as civil engineering, aerospace and specially in biomedical field [13–15]. The manufactured porous materials such as metal foams which own assemblages of both encouraging physical and mechanical properties have been commonly used in structural materials with lightweight [16, 17] and biomaterials [18]. The GPLs are spreaded in materials in order to alter the employment [19]. With the mixture advantages of both GPLs and porosities, the mechanical properties of the porous material are noticeably healthier but still retain their benefits. FGP-GPLs have been presented to achieve the needed mechanical characteristics based on the correcting the sizes [20–22]. In recent years, there are many works examined the influences of GPLs and porosities on the behaviors of plates and beams. It can be listed that Kitipornchai et al. [23] analyzed the free vibration of and elastic buckling for FGP beams reinforced by GPLs based on the Ritz method and Timoshenko beam theory. With the same used theories, Chen et al. [24] studied the nonlinear free vibration, post-buckling performances of FGP-GPLs beams. The uniaxial, biaxial, shear buckling and free vibration behaviors of FGP-GPLs plates were also examined by Yang et al. [25] based on FSDT and using Chebyshev-Ritz method. In addition, the static, free vibration and buckling of FGP-GPLs plates were also studied by Li et al. [26] using IGA based on both FSDT and TSDT.

Many plate theories are used to analyze behaviors of plate structures including CPT, FSDT and HSDT. Each plate theory has its advantages and disadvantages. However, different HSDTs have been proposed described by a transverse shear function in order to prove more advantages than CPT and FSDT. The transverse shear functions can illustrate the nonlinear of shear stresses across the thickness direction of plate. Some functions have been proposed and given well results such as polynomial, trigonometric and hyperbolic functions.

HSDT proves dominance in calculating the vibration responses of thin to thick plate structures. Since HSDTs have five or seven unknowns in approximated formulation, computational cost extensively rises with respect to DOFs. Hence, the reserachers have built a HSDT with only three variables. Moreover, a three-variable formulation allows us to analyze plates as the same way of 3D solid. The three-variable theories have been proposed by Endo et al. [27, 28] and by Senjanovic [29, 30] for the first time. Recently, a new three-variable shear deformation plate theory of FGM plates has been presented by Nguyen et al. [31] with the refined plate theory (RPT) is exploited. The relationship of bending and shear displacements is considered for all three-variable theories. However, the theory of Nguyen et al. [31] which is different to the previous works is using RPT. With RPT, calculation of plate problems accounts the shear stress impact without presence of a shear correction factor (SCF).

In this study, free vibration analysis of the FGP plates reinforced by GPLs is studied in combination of a generalized THSDT and IGA method. The generalized THSDT with arbitary transverse shear function shows high effectiveness in analyzing the behaviors of plate structures. The sides of the length-to-thickness ratio, porosity coefficient, different porosity distribution types, GPL distribution patterns and weight fraction of FGP-GPLs plates are also investigated and debated.

2. Mechanics of material for the FGP-GPLs plate

A FGP plate created from metal foams and reinforced by GPLs is illustrated as in Fig. 1, in which the length, the width and the thickness of plate are a, b and h, respectively.

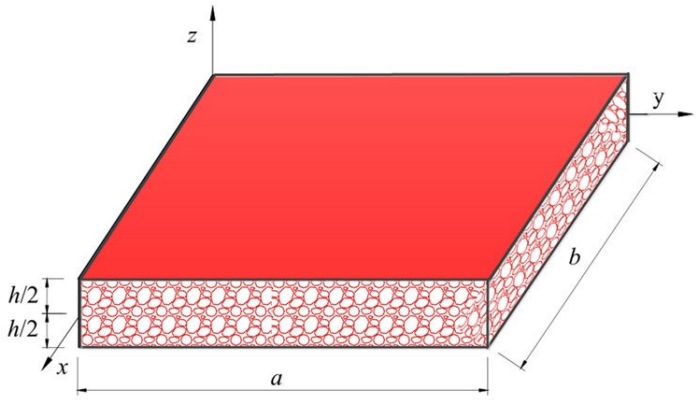

Figure 1. Configuration of an FGP-GPLs plate

Three different porosity distribution types along the thickness of plates including two types of non-uniformly symmetric and a uniform are shown in Fig. 2. As presented in this figure, E_1' is Young's modulus of uniform porosity distribution, E_1' and E_2' represent the maximum and minimum Young's moduli of the non-uniformly distributed porous material without GPLs, respectively. In addition, three distinctive GPL distribution patterns A, B and C depicted in Fig. 2 corresponds to three different types of porosity dispersion. In any pattern, the volume fraction V_{GPL} of GPLs varies smoothly in the direction of thickness. The symbol S_{ij} represents the maximum volume fraction, where $i = 1, 2, 3$ are three porosity distribution types and $j = 1, 2, 3$ imply three dispersion patterns, respectively.

The plate has the Young's moduli $E(z)$, shear modulus $G(z)$ and mass density $\rho(z)$ which change along the thickness direction for different porosity distribution types can be expressed as

$$\begin{cases} E(z) = E_1\left[1 - e_0\lambda(z)\right], \\ G(z) = E(z)/\left[2(1+\nu(z))\right], \\ \rho(z) = \rho_1\left[1 - e_m\lambda(z)\right], \end{cases} \tag{1}$$

where

$$\lambda(z) = \begin{cases} \cos(\pi z/h), & \text{Non-uniform porosity distribution 1} \\ \cos(\pi z/2h + \pi/4), & \text{Non-uniform porosity distribution 2} \\ \lambda, & \text{Uniform porosity distribution} \end{cases} \tag{2}$$

in which $E_1 = E_1'$ and $E_1 = E'$ for types of non-uniformly and uniform porosity distribution, respectively. ρ_1 denotes the maximum value of mass density of the porous core. The porosity coefficient e_0 can be determined by

$$e_0 = 1 - E_2'/E_1' \tag{3}$$

The mechanical properties of closed- cell cellular solids constructed by the Gaussian Random Field (GRF) scheme [32] are given as

$$\frac{E(z)}{E_1} = \left(\frac{\rho(z)/\rho_1 + 0.121}{1.121}\right)^{2.3} \text{ for } \left(0.15 < \frac{\rho(z)}{\rho_1} < 1\right) \tag{4}$$

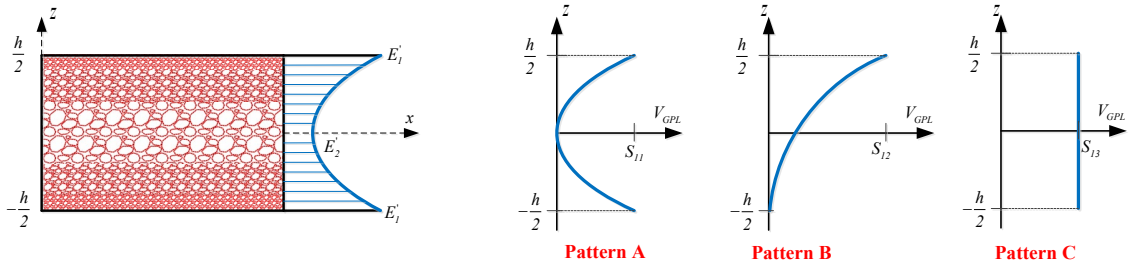

(a) Non-uniform porosity distribution 1

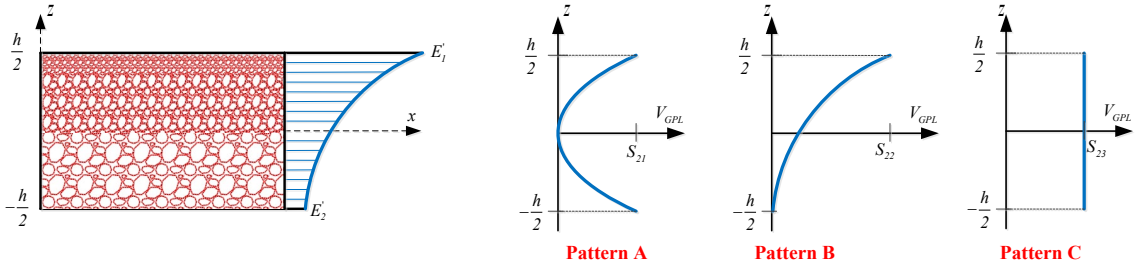

(b) Non-uniform porosity distribution 2

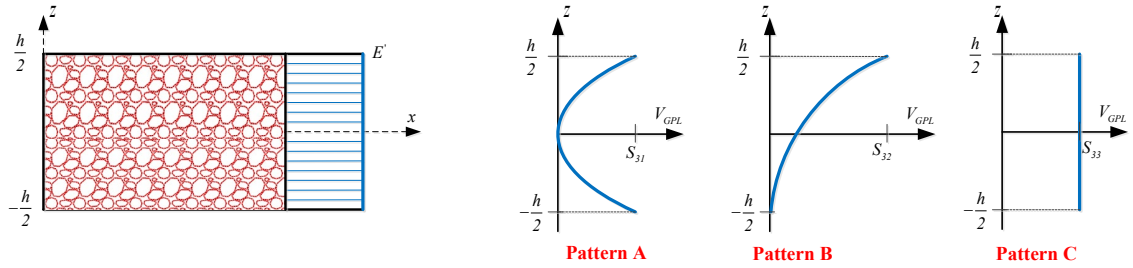

(c) Uniform porosity distribution

Figure 2. Three porosity distributions and three distinctive GPL distribution patterns

The coefficient of mass density e_m in Eq. (1) is probably identified as

$$e_m = \frac{1.121\left(1 - \sqrt[2.3]{1 - e_0\lambda(z)}\right)}{\lambda(z)} \tag{5}$$

Besides, Poisson's ratio $v(z)$ is described as

$$v(z) = 0.221p' + v_1(0.342p'^2 - 1.21p' + 1) \tag{6}$$

in which v_1 is the Poisson's ratio of the metal matrix no having pores porosities and p' is known as

$$p' = 1.121\left(1 - \sqrt[2.3]{1 - e_0\lambda(z)}\right) \tag{7}$$

In order to achieve a deep and reasonable comparison, the mass per unit of surface M of plates with numerous porosity distributions is built to be similar and can be computed by

$$M = \int_{-h/2}^{h/2} \rho(z)dz \tag{8}$$

Then, the coefficient λ in Eq. (2) for uniform porosity distribution is given as

$$\lambda = \frac{1}{e_0} - \frac{1}{e_0}\left(\frac{M/\rho_1 h + 0.121}{0.121}\right)^{2.3} \tag{9}$$

For three dispersion patterns, the volume fraction of GPLs shown in Fig. 2 can be presented as

$$V_{GPL} = \begin{cases} S_{i1}\left[1 - \cos(\pi z/h)\right], & \text{Pattern A} \\ S_{i2}\left[1 - \cos(\pi z/2h + \pi/4)\right], & \text{Pattern B} \\ S_{i3}, & \text{Pattern C} \end{cases} \tag{10}$$

The volume fraction V_{GPL} and weight fractions Λ_{GPL} have the relationship together through equation as

$$\frac{\Lambda_{GPL}\rho_m}{\Lambda_{GPL}\rho_m + \rho_{GPL} - \Lambda_{GPL}\rho_{GPL}} \int_{-\frac{h}{2}}^{\frac{h}{2}} \left[1 - e_m\lambda(z)\right]dz = \int_{-\frac{h}{2}}^{\frac{h}{2}} V_{GPL}\left[1 - e_m\lambda(z)\right]dz \tag{11}$$

The Halpin-Tsai micromechanical model presents the Young's modulus, E_1, written as

$$E_1 = \frac{3}{8}\left(\frac{1 + \zeta_L\eta_L V_{GPL}}{1 - \eta_L V_{GPL}}\right)E_m + \frac{5}{8}\left(\frac{1 + \zeta_{\mathrm{w}}\eta_{\mathrm{w}} V_{GPL}}{1 - \eta_{\mathrm{w}} V_{GPL}}\right)E_m \tag{12}$$

in which

$$\zeta_L = \frac{2l_{GPL}}{t_{GPL}}, \quad \zeta_{\mathrm{w}} = \frac{2w_{GPL}}{t_{GPL}}, \quad \eta_L = \frac{(E_{GPL}/E_m) - 1}{(E_{GPL}/E_m) + \zeta_L}, \quad \eta_{\mathrm{w}} = \frac{(E_{GPL}/E_m) - 1}{(E_{GPL}/E_m) + \zeta_w} \tag{13}$$

where w_{GPL}, l_{GPL} and t_{GPL} imply the average width, length and thickness of graphene platelets, respectively; E_m and E_{GPL} are Young's moduli of metal matrix and graphene platelets, respectively. For metal matrix with the presence of porosities, the mass density ρ_1 and Poison's ratio ν_1 of the GPLs are defined through the rule of mixture as

$$\rho_1 = \rho_{GPL}V_{GPL} + \rho_m V_m \tag{14}$$

$$\nu_1 = \nu_{GPL}V_{GPL} + \nu_m V_m \tag{15}$$

where ρ_{GPL} and ν_{GPL} symbolize the mass density and Poisson's ratio of GPLs, respectively; while ρ_m, ν_m and $V_m = 1 - V_{GPL}$ denote the mass density, Poisson's ratio and volume fraction of metal matrix, respectively.

3. Theory and approximation of FGP-GPLs plate

3.1. A generalized three-variable high order shear deformation theory (THSDT)

The displacements of a random point in plate according to THSDT is written as [31]

$$\begin{aligned} u(x,y,z) &= u_0 - z\frac{\partial w_0}{\partial x} + c_f f(z)\frac{\partial}{\partial x}\Delta w_0 \\ v(x,y,z) &= v_0 - z\frac{\partial w_0}{\partial y} + c_f f(z)\frac{\partial}{\partial y}\Delta w_0 \\ w(x,y,z) &= w_0 + c_f \Delta w_0 \end{aligned} \tag{16}$$

Table 1. The list of common functions $f(z)$

Name	Function $f(z)$	Source
Case 1	$f(z) = 0$	FSDT [33]
Case 2	$f(z) = \dfrac{-4z^3}{3h^2}$	TSDT [34]
Case 3	$f(z) = \dfrac{-z}{8} - \dfrac{2z^3}{h^2} + \dfrac{2z^5}{h^4}$	HSDT [35]
Case 4	$f(z) = \tan^{-1}\left(\sin\dfrac{\pi z}{h}\right) - z$	HSDT [36]

where u_0, v_0 are displacements in plane, w_0 represents displacement through the thickness direction, $\Delta = \partial^2_{,x^2} + \partial^2_{,y^2}$ is the Laplace operator and c_f is a correction factor of the shear displacement which is set later. The nonlinear distribution of some odd functions $f(z)$ based on the generalized three-variable high order shear deformation theory is given in Table 1.

The relationship between strain and displacement fields is computed as follows

$$\begin{Bmatrix} \varepsilon_{xx} \\ \varepsilon_{yy} \\ \gamma_{xy} \end{Bmatrix} = \begin{Bmatrix} \dfrac{\partial u_0}{\partial x} \\ \dfrac{\partial v_0}{\partial y} \\ \dfrac{\partial u_0}{\partial y} + \dfrac{\partial v_0}{\partial x} \end{Bmatrix} - z \begin{Bmatrix} \dfrac{\partial^2 w_0}{\partial x^2} \\ \dfrac{\partial^2 w_0}{\partial y^2} \\ 2\dfrac{\partial^2 w_0}{\partial x \partial y} \end{Bmatrix} + c_f f(z) \begin{Bmatrix} \dfrac{\partial^2}{\partial x^2}\Delta w_0 \\ \dfrac{\partial^2}{\partial y^2}\Delta w_0 \\ 2\dfrac{\partial^2}{\partial x \partial y}\Delta w_0 \end{Bmatrix} \tag{17a}$$

$$= \boldsymbol{\varepsilon}_0 + z\boldsymbol{\varepsilon}_1 + f(z)\boldsymbol{\varepsilon}_2 \tag{17b}$$

$$\begin{Bmatrix} \gamma_{xz} \\ \gamma_{yz} \end{Bmatrix} = c_f\left(1 + f(z)_{,z}\right) \begin{Bmatrix} \dfrac{\partial}{\partial x} \\ \dfrac{\partial}{\partial y} \end{Bmatrix} \Delta w_0 = c_f\left(1 + f(z)_{,z}\right)\boldsymbol{\varepsilon}_z \tag{17c}$$

The resultants are stated as follows

$$\begin{bmatrix} N_{xx} & N_{yy} & N_{xy} \end{bmatrix}^T = \mathbf{A}\boldsymbol{\varepsilon}_0 + \mathbf{B}\boldsymbol{\varepsilon}_1 + \mathbf{E}\boldsymbol{\varepsilon}_2 \tag{18a}$$

$$\begin{bmatrix} M_{xx} & M_{yy} & M_{xy} \end{bmatrix}^T = \mathbf{B}\boldsymbol{\varepsilon}_0 + \mathbf{D}\boldsymbol{\varepsilon}_1 + \mathbf{F}\boldsymbol{\varepsilon}_2 \tag{18b}$$

$$\begin{bmatrix} Q_{13} & Q_{23} \end{bmatrix}^T = \mathbf{D}^s\boldsymbol{\varepsilon}_s \tag{18c}$$

where

$$\begin{aligned} (\mathbf{A}, \mathbf{B}, \mathbf{D}, \mathbf{E}, \mathbf{F}) &= \int_{-h/2}^{h/2} \left[1, z, z^2, c_f f(z), c_f z f(z)\right]\mathbf{C}_b dz \\ \mathbf{D}^s &= \int_{-h/2}^{h/2} c_f\left(1 + f(z)_{,z}\right)\mathbf{C}_s dz \end{aligned} \tag{19}$$

and

$$\mathbf{C}_b = \begin{bmatrix} C_{11} & C_{12} & 0 \\ C_{12} & C_{22} & 0 \\ 0 & 0 & C_{66} \end{bmatrix}; \quad \mathbf{C}_s = \begin{bmatrix} C_{55} & 0 \\ 0 & C_{44} \end{bmatrix} \tag{20}$$

where the correction factors c_f based on the Laplacian of bending displacement w_0 [31] is calculated as

$$c_f = \frac{z_0 \int_{-h/2}^{h/2} \frac{zE(z)}{1-\upsilon^2} dz - \int_{-h/2}^{h/2} \frac{z^2 E(z)}{1-\upsilon^2} dz}{\int_{-h/2}^{h/2} \left(1 + f(z)_{,z}\right) \frac{E(z)}{2(1+\upsilon)} dz} \tag{21}$$

in which z_0 is the distance from the central plane to the neutral plane of the plate and is expressed as follows:

$$z_0 = \frac{\int_{-h/2}^{h/2} zE(z)dz}{\int_{-h/2}^{h/2} E(z)dz} \tag{22}$$

3.2. Garlerkin weak forms of FGP-GPL plates

For free vibration analysis, the weak form is determined as

$$\int_V \begin{bmatrix} \varepsilon_{xx} \\ \varepsilon_{yy} \\ \gamma_{xy} \end{bmatrix}^T \mathbf{C}_b \begin{bmatrix} \varepsilon_{xx} \\ \varepsilon_{yy} \\ \gamma_{xy} \end{bmatrix} dV + \int_V \begin{bmatrix} \gamma_{xz} \\ \gamma_{yz} \end{bmatrix}^T \mathbf{C}_s \begin{bmatrix} \gamma_{xz} \\ \gamma_{yz} \end{bmatrix} dV + \int_\Omega \delta\tilde{\mathbf{u}}^T \bar{\mathbf{m}} \ddot{\tilde{\mathbf{u}}} d\Omega = 0 \tag{23}$$

Then, setting Eq. (17) into Eq. (23) and remarking that I_3 is a unit matrix of size 3×3, it can be obtained

$$\begin{aligned} &\int_\Omega \begin{bmatrix} \boldsymbol{\varepsilon}_0 \\ \boldsymbol{\varepsilon}_1 \\ \boldsymbol{\varepsilon}_2 \end{bmatrix}^T \left\{ \int_{-h/2}^{h/2} \begin{bmatrix} \mathbf{I}_3 \\ z\mathbf{I}_3 \\ c_f f(z)\mathbf{I}_3 \end{bmatrix} \mathbf{C}_b \begin{bmatrix} \mathbf{I}_3 & z\mathbf{I}_3 & c_f f(z)\mathbf{I}_3 \end{bmatrix} dz \right\} \begin{bmatrix} \boldsymbol{\varepsilon}_0 \\ \boldsymbol{\varepsilon}_1 \\ \boldsymbol{\varepsilon}_2 \end{bmatrix} d\Omega \\ &+ \int_\Omega \boldsymbol{\varepsilon}_s^T \left\{ \int_{-h/2}^{h/2} c_f \left(1 + f(z)_{,z}\right) \mathbf{C}_s \left(1 + f(z)_{,z}\right) dz \right\} \boldsymbol{\varepsilon}_s d\Omega + \int_\Omega \delta\tilde{\mathbf{u}}^T \bar{\mathbf{m}} \ddot{\tilde{\mathbf{u}}} d\Omega = 0 \end{aligned} \tag{24}$$

Eq. (24) can be rewritten as below

$$\int_\Omega \left\{ \begin{bmatrix} \boldsymbol{\varepsilon}_0 \\ \boldsymbol{\varepsilon}_1 \\ \boldsymbol{\varepsilon}_2 \end{bmatrix}^T \begin{bmatrix} \mathbf{A} & \mathbf{B} & \mathbf{E} \\ \mathbf{B} & \mathbf{D} & \mathbf{F} \\ \mathbf{E} & \mathbf{F} & \tilde{\mathbf{H}} \end{bmatrix} \begin{bmatrix} \boldsymbol{\varepsilon}_0 \\ \boldsymbol{\varepsilon}_1 \\ \boldsymbol{\varepsilon}_2 \end{bmatrix} + \boldsymbol{\varepsilon}_s^T \tilde{\mathbf{D}}^s \boldsymbol{\varepsilon}_s \right\} d\Omega + \int_\Omega \delta\tilde{\mathbf{u}}^T \begin{bmatrix} I_1 & I_2 & I_4 \\ I_2 & I_3 & I_5 \\ I_4 & I_5 & I_6 \end{bmatrix} \ddot{\tilde{\mathbf{u}}} d\Omega = 0 \tag{25}$$

where

$$\begin{aligned} \tilde{\mathbf{H}} &= \int_{-h/2}^{h/2} \left[c_f^2 f^2(z)\right] \mathbf{C}_b dz, \quad \tilde{\mathbf{D}}^s = \int_{-h/2}^{h/2} c_f^2 \left(1 + f(z)_{,z}\right)^2 \mathbf{C}_s dz, \\ (I_1, I_2, I_3, I_4, I_5, I_6) &= \int_{-h/2}^{h/2} \rho(z) \left[1, z, z^2, c_f f(z), c_f z f(z), c_f^2 f^2(z)\right] dz \end{aligned} \tag{26}$$

and

$$\tilde{\mathbf{u}} = \begin{Bmatrix} \mathbf{u}_1 \\ \mathbf{u}_2 \\ \mathbf{u}_3 \end{Bmatrix}; \quad \mathbf{u}_1 = \begin{Bmatrix} u_0 \\ v_0 \\ w_0 \end{Bmatrix}; \quad \mathbf{u}_2 = \begin{Bmatrix} -\frac{\partial w_0}{\partial x} \\ -\frac{\partial w_0}{\partial y} \\ 0 \end{Bmatrix}; \quad \mathbf{u}_3 = \begin{Bmatrix} \frac{\partial}{\partial x}\Delta w_0 \\ \frac{\partial}{\partial y}\Delta w_0 \\ \Delta w_0 \end{Bmatrix} \tag{27}$$

3.3. Isogeometric analysis (IGA) for THSDT

With IGA, we use the NURBS basis function (Non-Uniform Rational B-splines) to approximate. The displacement field of the FGP plate can be approached as follows

$$\mathbf{u}^h(\xi,\eta) = \sum_{A}^{m\times n} R_A^e(\xi,\eta)\mathbf{d}_A \tag{28}$$

where $R_A^e(\xi,\eta)$ expresses a NURBS basis function, m×n is the number of basis functions and d_A is the vector of nodal degrees of freedom related to control point A.

The in-plane and shear strains can be rewritten as

$$\begin{bmatrix} \boldsymbol{\varepsilon}_0 & \boldsymbol{\varepsilon}_1 & \boldsymbol{\varepsilon}_2 \end{bmatrix}^T = \sum_{A=1}^{m\times n} \begin{bmatrix} \mathbf{B}_0 & \mathbf{B}_1 & \mathbf{B}_2 \end{bmatrix}^T \mathbf{d}_A, \quad \boldsymbol{\varepsilon}_s = \sum_{A=1}^{m\times n} \mathbf{B}_s \mathbf{d}_A \tag{29}$$

where

$$\begin{aligned} \mathbf{B}_0 &= \begin{bmatrix} \dfrac{\partial R_A}{\partial x} & 0 & 0 \\ 0 & \dfrac{\partial R_A}{\partial y} & 0 \\ \dfrac{\partial R_A}{\partial y} & \dfrac{\partial R_A}{\partial x} & 0 \end{bmatrix}, \quad \mathbf{B}_1 = -\begin{bmatrix} 0 & 0 & \dfrac{\partial^2 R_A}{\partial x^2} \\ 0 & 0 & \dfrac{\partial^2 R_A}{\partial y^2} \\ 0 & 0 & 2\dfrac{\partial^2 R_A}{\partial x \partial y} \end{bmatrix}, \\ \mathbf{B}_2 &= \begin{bmatrix} 0 & 0 & \dfrac{\partial^2}{\partial x^2}\Delta R_A \\ 0 & 0 & \dfrac{\partial^2}{\partial y^2}\Delta R_A \\ 0 & 0 & 2\dfrac{\partial^2}{\partial x \partial y}\Delta R_A \end{bmatrix}, \quad \mathbf{B}_s = \begin{bmatrix} 0 & 0 & \dfrac{\partial}{\partial x}\Delta R_A \\ 0 & 0 & \dfrac{\partial}{\partial x}\Delta R_A \end{bmatrix} \end{aligned} \tag{30}$$

By replacing Eq. (28) for displacement field u_i $(i = 1, 2, 3)$ in Eq. (27), u_i can be written as follows

$$\begin{bmatrix} \mathbf{u}_1 & \mathbf{u}_2 & \mathbf{u}_3 \end{bmatrix}^T = \sum_{A=1}^{m\times n} \begin{bmatrix} \mathbf{N}_1 & \mathbf{N}_2 & \mathbf{N}_3 \end{bmatrix}^T \mathbf{d}_A \tag{31}$$

in which

$$\begin{aligned} \mathbf{N}_1 &= \begin{bmatrix} R_A & 0 & 0 \\ 0 & R_A & 0 \\ 0 & 0 & R_A \end{bmatrix}; \quad \mathbf{N}_2 = -\begin{bmatrix} 0 & 0 & R_{A,x} \\ 0 & 0 & R_{A,y} \\ 0 & 0 & 0 \end{bmatrix}; \\ \mathbf{N}_3 &= -\begin{bmatrix} 0 & 0 & \dfrac{\partial}{\partial x}\Delta R_A \\ 0 & 0 & \dfrac{\partial}{\partial y}\Delta R_A \\ 0 & 0 & 0 \end{bmatrix} + \begin{bmatrix} 0 & 0 & 0 \\ 0 & 0 & 0 \\ 0 & 0 & \Delta R_A \end{bmatrix} \end{aligned} \tag{32}$$

3.4. Governing equations of motion

The fundamental governing equation of free vibration analysis can be resulted in the following form

$$\left(\mathbf{K} - \omega^2 \mathbf{M}\right)\mathbf{d} = 0 \tag{33}$$

where $\mathbf{K}$ is the global stiffness matrix and is given by

$$\mathbf{K} = \int_{\Omega} \left[\begin{Bmatrix} \mathbf{B}_1 \\ \mathbf{B}_2 \\ \mathbf{B}_3 \end{Bmatrix}^T \begin{bmatrix} \mathbf{A} & \mathbf{B} & \mathbf{E} \\ \mathbf{B} & \mathbf{D} & \mathbf{F} \\ \mathbf{E} & \mathbf{F} & \tilde{\mathbf{H}} \end{bmatrix} \begin{Bmatrix} \mathbf{B}_1 \\ \mathbf{B}_2 \\ \mathbf{B}_3 \end{Bmatrix} + \mathbf{B}_s^T \tilde{\mathbf{D}}^s \mathbf{B}_s \right] d\Omega \tag{34}$$

And $\mathbf{M}$ is the global mass matrix. It is defined as

$$\mathbf{M} = \int_{\Omega} \left\{ \begin{Bmatrix} \mathbf{N}_1 \\ \mathbf{N}_2 \\ \mathbf{N}_3 \end{Bmatrix}^T \begin{bmatrix} \mathbf{I}_1 & \mathbf{I}_2 & \mathbf{I}_4 \\ \mathbf{I}_2 & \mathbf{I}_3 & \mathbf{I}_5 \\ \mathbf{I}_4 & \mathbf{I}_5 & \mathbf{I}_6 \end{bmatrix} \begin{Bmatrix} \mathbf{N}_1 \\ \mathbf{N}_2 \\ \mathbf{N}_3 \end{Bmatrix} \right\} d\Omega \tag{35}$$

3.5. Imposing essential boundary conditions

For the set of boundary conditions (BCs), the employment of two standard BCs for a rectangular plate are deliberated in this section as follows:

- Simply supported:

At $x = 0, a$:

$$v_0 = 0 \tag{36a}$$

$$w_0 + \alpha \Delta^2 w_0 = 0 \tag{36b}$$

At $y = 0, b$:

$$u_0 = 0 \tag{37a}$$

$$w_0 + \alpha \Delta^2 w_0 = 0 \tag{37b}$$

- Clamped:

At $x = 0, a$:

$$u_0 = 0; v_0 = 0 \tag{38a}$$

$$w_0 + \alpha \Delta^2 w_0 = 0; \quad \frac{\partial w_0}{\partial x} - \gamma \frac{\partial}{\partial x} \Delta^2 w_0 \tag{38b}$$

At $y = 0, b$:

$$u_0 = 0; v_0 = 0 \tag{39a}$$

$$w_0 + \alpha \Delta^2 w_0 = 0; \quad \frac{\partial w_0}{\partial y} - \gamma \frac{\partial}{\partial y} \Delta^2 w_0 \tag{39b}$$

Eqs. (36a), (37a), (38a) and (39a) are the classical BCs while Eqs. (36b), (37b), (38b) and (39b) are the non-classical BCs. The classical BCs are able to directly force into the system equations like as all papers related to IGA. For the non-classical BCs, the penalty method is used, referring to [31] for more details.

4. Numerical results

4.1. Convergence and verification analyses

We first consider a square functionally graded material (FGM) Al/Al_2O_3 plate with length-to-thickness ratio $a/h = 100$ in order to prove and clarify the convergence of the proposed approach. The FGM plate is subjected to SSSS and CCCC BCs. The properties of component materials can be reviewed in Table 2. The non-dimensional frequencies are given $\varpi = \omega\pi^2\left(a^2/h\right)\sqrt{\frac{\rho_m}{E_m}}$ in which the subscript "m" indicates the metal elements and ω is the nominal natural frequencies of the FGM plate. Table 3 illustrates the convergence of the first lowest frequency with respect to given meshes for all cases. The obtained results are compared to exact solutions studied by Baferani et al. [37], a mesh of 11×11 can be selected for analysis. In addition, the case 4 has more a good agreement than other cases as well as closest to exact solutions. Therefore, case 4 is chosen to run the result of the first five lowest frequencies for SSSS and CCCC Bcs in Tables 4 and 5, respectively. The present results for SSSS plate are evaluated with those of the IGA based on FSDT and TSDT [26], the IGA using simple FSDT proposed by Yin et al. (IGA-SFSDT) [38] and exact solutions [37]. For CCCC plate, because there are not exact solutions the solutions are futher compared to IGA based on classical plate theory (CPT) and physical neutral surface [39] (IGA-CPT-neu). It can be seen that all cases match excellent compared to the published results. These reference solutions use IGA with FSDT or TSDT for five DOFs for each node (control point). Althought the proposed method only has three DOFs per node, there is a good agreement between the present work with those of the exact solutions. Moreover, an increasing of gradient index leads to a decreasing of natural frequency of plate due to reducing of the stiffness's plate.

Table 2. Material properties

Material	E (GPa)	ρ (kg/m^3)	ν
Aluminum (Al)	70	2702	0.3
Alumina (Al/Al_2O_3)	380	3800	0.3
Copper	130	8960	0.34
GPL	1010	1062.5	0.186

Table 3. Influence of the mesh levels on the frequency parameter ϖ of a FGM square plate with SSSS BCs ($a/h = 100$)

Mesh	Case 1	Case 2	Case 3	Case 4
7×7	115.9056	115.9136	115.9095	115.8692
11×11	115.8702	115.8693	115.8688	115.8696
15×15	115.8703	115.8693	115.8688	115.8697
Exact [38]	115.8695			

Table 4. The first five normalized natural frequencies ϖ of a FGM square plate with SSSS BCs

Gradient index, n	Method	Mode 1	Mode 2	Mode 3	Mode 4	Mode 5
0	IGA-FSDT [26]	115.9056	289.7465	289.7465	463.2783	579.6187
	IGA-TSDT [26]	115.9136	289.8146	289.8146	463.4071	579.9500
	IGA-SFSDT [38]	115.8926	289.5800	289.5806	463.0741	579.7215
	Exact [37]	115.8695	289.7708	-	463.4781	-
	Present (Case 4)	115.8696	289.7824	289.6212	463.4521	579.7822
0.5	IGA-FSDT [26]	98.1469	245.3765	245.3765	392.3437	490.9582
	IGA-TSDT [26]	98.1538	245.4364	245.4364	392.4539	491.2537
	IGA-SFSDT [38]	98.1343	245.2169	245.2169	392.1448	490.0963
	Exact [37]	98.0136	245.3251	-	392.4425	-
	Present (Case 4)	98.0139	245.3192	245.3361	392.4489	491.0025
1	IGA-FSDT [26]	88.4403	221.1177	221.1177	353.5548	442.4573
	IGA-TSDT [26]	88.4467	221.1738	221.1738	353.6574	442.7351
	IGA-SFSDT [38]	88.4280	220.9643	220.9643	353.3613	441.6348
	Exact [37]	88.3093	221.0643	-	392.4425	-
	Present (Case 4)	88.3089	220.9521	221.1542	373.5044	441.7015
2	IGA-FSDT [26]	80.4065	201.0261	201.0261	321.4234	402.2333
	IGA-TSDT [26]	80.4126	201.0782	201.0782	321.5199	402.4897
	IGA-SFSDT [38]	80.3953	200.8879	200.8879	321.2475	401.5008
	Exact [37]	80.3517	200.8793	-	321.4069	-
	Present (Case 4)	80.3522	200.8811	201.0845	321.4111	401.6012

Table 5. The first five normalized natural frequencies ϖ of a FGM square plate with CCCC BCs

Gradient index, n	Method	Mode 1	Mode 2	Mode 3	Mode 4	Mode 5
0	IGA-FSDT [26]	211.3331	431.0821	431.0821	635.0710	773.2417
	IGA-TSDT [26]	211.4169	431.3977	431.3977	635.6156	774.2260
	IGA-SFSDT [38]	211.1468	430.3633	430.3633	634.1625	770.8950
	IGA-CPT-neu [39]	211.3372	431.0061	431.0061	635.4464	772.7523
	Present (Case 4)	211.3219	431.1210	431.1210	635.5945	773.1454
0.5	IGA-FSDT [26]	178.9901	365.1828	365.1828	538.0286	655.2518
	IGA-TSDT [26]	179.0627	365.4593	365.4593	538.4984	656.1226
	IGA-SFSDT [38]	178.8047	364.4639	364.4639	537.0816	652.9193
	IGA-CPT-neu [39]	178.9493	364.9528	364.9528	538.0607	654.3228
	Present (Case 4)	178.9399	365.0012	365.0012	538.4877	656.2542
1	IGA-FSDT [26]	161.3043	329.1291	329.1291	484.9212	590.6464
	IGA-TSDT [26]	161.3711	329.3850	329.3850	485.3539	591.4565
	IGA-SFSDT [38]	161.1242	328.4308	328.4308	483.9866	588.3962
	IGA-CPT-neu [39]	161.2484	328.8502	328.8502	484.8293	589.5860
	Present (Case 4)	161.2459	329.0142	329.0142	484.8752	590.2201
2	IGA-FSDT [26]	146.6479	299.2113	299.2113	440.8304	536.9202
	IGA-TSDT [26]	146.7089	299.4452	299.4452	441.2281	537.6605
	IGA-SFSDT [38]	146.4868	298.5884	298.5884	439.9988	534.9293
	IGA-CPT-neu [39]	146.6016	298.9753	298.9753	440.7781	536.0119
	Present (Case 4)	146.6152	299.0114	299.0114	441.1233	537.1687

4.2. FGP-GPLs plates

A FGP-GPLs plate is considered with matrix material made of copper. Table 2 shows the material properties of copper and graphene platelets. GPLs have w_{GPL} = 1.5 μm, l_{GPL} = 2.5 μm

and t_{GPL} = 1.5 nm which are defined in Eq. (13). The fundamental frequency is described as $\omega^* = \omega a\sqrt{\frac{\rho_m(1-\nu_m^2)}{E_m}}$. Table 6 indicates the frequency parameters of a square FGP plate affected by the length-to-thickness ratio (a/h), weight fraction Λ_{GPL} = 1 $wt.\%$ and porosity coefficient e_0 = 0.5. Values in parentheses are % errors. Through our observation, the present results show a great likeness with small erroneousness when compared to the obtained results in Ref. [25] examined by Yang et al. based on Chebyshev-Ritz method. Clearly, at a specific of weight fraction the plate's stiffness decreases notably as the higher length-to-thickness ratio and leads to a reduction of the fundamental frequency for both porosity distribution 1 and uniform porosity with SSSS and CCCC BCs.

Table 6. Influence of the ratio a/h on dimensionless fundamental natural frequencies of a square FGP-GPLs plate (case 4, Λ_{GPL} = 1 $wt.\%$, e_0 = 0.5)

	a/h		Porosity distribution 1			Uniform porosity		
			GPL A	GPL B	GPL C	GPL A	GPL B	GPL C
SSSS	20	Ref. [25]	0.3958	-	0.3574	0.3627	-	0.3252
		Present	0.3958	0.3497	0.3570	0.3620	0.3188	0.3238
			(0.00)	-	(−0.10)	(−0.21)	-	(−0.44)
	30	Ref. [25]	0.2657	-	0.2397	0.2433	-	0.2179
		Present	0.2663	0.2346	0.2396	0.2430	0.2136	0.2169
			(0.24)	-	(−0.06)	(−0.14)	-	(−0.47)
	40	Ref. [25]	0.1997	-	0.1801	0.1828	-	0.1637
		Present	0.2004	0.1764	0.1801	0.1827	0.1605	0.1629
			(0.35)	-	(−0.02)	(−0.07)	-	(−0.47)
	50	Ref. [25]	0.1600	-	0.1442	0.1464	-	0.1311
		Present	0.1606	0.1413	0.1442	0.1463	0.1285	0.1304
			(0.36)	-	(0.00)	(−0.07)	-	(−0.50)
CCCC	20	Ref. [25]	0.7022	-	0.6366	0.6456	-	0.5814
		Present	0.6940	0.6191	0.6318	0.6394	0.5681	0.5767
			(−1.17)	-	(−0.76)	(−0.96)	-	(−0.80)
	30	Ref. [25]	0.4783	-	0.4324	0.4387	-	0.3938
		Present	0.4767	0.4220	0.4307	0.4365	0.3854	0.3912
			(−0.33)	-	(−0.38)	(−0.50)	-	(−0.65)
	40	Ref. [25]	0.3616	-	0.3265	0.3313	-	0.2971
		Present	0.3615	0.3191	0.3257	0.3302	0.2908	0.2953
			(−0.02)	-	(−0.24)	(−0.32)	-	(−0.62)
	50	Ref. [25]	0.2904	-	0.2620	0.2659	-	0.2383
		Present	0.2907	0.2562	0.2616	0.2653	0.2333	0.2369
			(0.12)	-	(−0.16)	(−0.23)	-	(−0.59)

Values in parentheses are % errors

The impact of the coefficient of porosity e_0, weight fraction Λ_{GPL} and the GPLs dispersion patterns on the dimensionless frequencies of FGP-GPLs with several porosity distribution types are also displayed in the Table 7. It can be realized that the influence of porosity coefficient on the dimensionless frequencies is remarkable. When a larger size of internal pores, the fundamental frequency decreases due to a lessening in the stiffness of FGP plate. Clearly, with non-uniform porosity distribution 1, the obtained results marginally decrease. However, there is a strong decrease for the non-

uniform porosity distribution 2 and uniform porosity distribution. Of course, the obtained results also increase significantly when there is an increasing in weight fraction Λ_{GPL} from 0.5 *wt.%* to 1 *wt.%*. The careful observation shows that, frequency corresponding to pattern A distributed GPLs symmetrically through the midplane of plate offers the highest values, next is pattern C while the asymmetric dispersion pattern B has the smallest frequency. It means that for the same type of porosity distribution, the rigidity of the porous plates with pattern GPL A is maximum and the minimum is pattern GPL B. As a result, the dispersion pattern A yields the best reinforcing performance for the vibration analysis of GPLs plate. Besides, with arbitrary the GPLs dispersion patterns, weight fractions and porosity coefficients, the type of the porosity distribution 1 constantly supplies the best stiffness as verified by achieving the biggest frequency. It is possible to realize that the grouping between the porosity distribution 1 and GPL dispersion pattern A creates the excellent behaviors for FG porous structures compared with all studied combinations. The first six mode shapes of FGP-GPLs plate are also drawn in Fig. 3.

Table 7. Influence of porosity coefficient, type of porosity distribution, weight fraction Λ_{GPL} and GPLs dispersion patterns on dimensionless fundamental natural frequencies of a square FGP-GPLs plate

e_0	Porosity distribution 1			Porosity distribution 2			Uniform porosity		
	GPL A	GPL B	GPL C	GPL A	GPL B	GPL C	GPL A	GPL B	GPL C
0.1	0.6131	0.5735	0.5737	0.6062	0.5658	0.5670	0.5990	0.5585	0.5588
0.3	0.6076	0.5689	0.5695	0.5832	0.5420	0.5458	0.5871	0.5505	0.5503
0.5	0.6037	0.5662	0.5674	0.5532	0.5116	0.5185	0.5711	0.5394	0.5390
0.1	0.7062	0.6286	0.6386	0.6986	0.6199	0.6312	0.6973	0.6205	0.6299
0.3	0.6995	0.6229	0.6340	0.6721	0.5924	0.6077	0.6701	0.5959	0.6049
0.5	0.6940	0.6191	0.6318	0.6372	0.5578	0.5777	0.6394	0.5861	0.5767

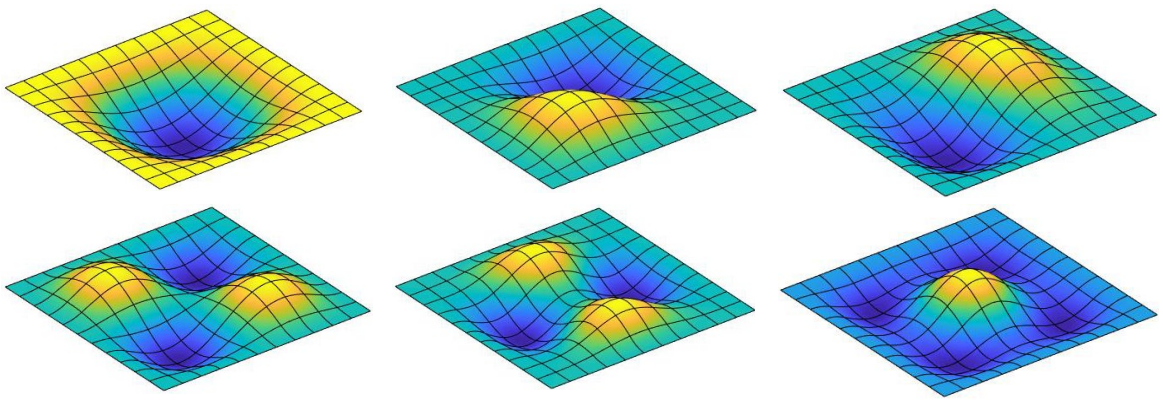

Figure 3. The first six mode shapes of of a square FGP-GPLs plate, CCCC BCs

The impact of the coefficient of porosity e_0, weight fraction Λ_{GPL} and the GPLs dispersion patterns on the dimensionless fundamental frequency of FGP plates with different porosity distribution types are also shown in Table 7. It can be seen that the effect of porosity coefficient on the dimensionless fundamental frequency is remarkable. When a larger size of internal pores, the fundamental frequency decreases due to a lessening in the stiffness of FGP plate. Clearly, with non-uniform porosity distribution 1, the results of the dimensionless fundamental frequency slightly decrease. However,

there is a more pronounced decrease in two cases of the non-uniform porosity distribution 2 and uniform porosity distribution. Of course, the obtained results also increase significantly when there is an increasing in weight fraction Λ_{GPL} from 0.5 wt.% to 1 wt.%. The careful observation shows that, frequency corresponding to pattern A distributed GPLs symmetrically through the midplane of plate provides the highest values, next is pattern C while the asymmetric dispersion pattern B has the lowest frequency. It means that for the same type of porosity distribution, the rigidity of the porous plates with pattern GPL A is maximum and the minimum is pattern GPL B. As a result, the dispersion pattern A yields the best reinforcing performance for the vibration analysis of GPLs plate. Besides, for any specific weight fractions, the GPLs dispersion patterns, and porosity coefficients, the porosity distribution 1 always provides the best stiffness as evidenced by obtaining the largest frequency. Possibly to see that the combination between the porosity distribution 1 and GPL dispersion pattern A makes the best structural behaivors for FG porous square plate compared with all considered combinations. The first six mode shapes of FGP-GPLs plate are also plotted in Fig. 3.

5. Conclusions

A valuable numerical approach within the outline of IGA based on the THSDT has been proposed for the frequency responses of FGP-GPLs plates. The three-variable high order shear deformation theory (THSDT) which satisfies CPT, FSDT and HSDT shows the strong efficiency for vibration problems. An investigation of three porosity distribution types and dispersion pattern of GPLs in plate in terms of free vibration is studied. The influence of different parameters on the behaviors of FGP-GPLs plates are exhaustively examined. Remarkably, the obtained results match well with current studies or available answers in the literature. Some several main remarks can be made:

1. Only adding a little the GPLs, the FGP plate's stiffness can be extensively increased. Therefore, for any defined porosity coefficient, by rising the weight fraction of the GPLs, the natural frequency would be enlarged.

2. An expanding of the porosity coefficient causes to the ability of reducing the stiffness of structures. Thus, for a given weight fraction, by growing the porosity coefficient, the obtained results of frequency would be compressed.

3. The dispersion pattern of the GPLs also has remarkble impact on the behaviors of the FG porous plate. Among all studied cases, the combination of the non-uniform porosity distribution 1 and dispersion pattern A gives the largest solutions. That is, it can become a best reinforcement candidate for the vibration analysis problem of the FGP plate.

Acknowledgment

This research is funded by Ho Chi Minh City University of Technology and Education (HCMUTE) under grant number T2020-89TĐ.

References

[1] Tampieri, A., Celotti, G., Sprio, S., Delcogliano, A., Franzese, S. (2001). Porosity-graded hydroxyapatite ceramics to replace natural bone. *Biomaterials*, 22(11):1365–1370.

[2] Pompe, W., Worch, H., Epple, M., Friess, W., Gelinsky, M., Greil, P., Hempel, U., Scharnweber, D., Schulte, K. J. M. S. (2003). Functionally graded materials for biomedical applications. *Materials Science and Engineering: A*, 362(1-2):40–60.

[3] Lefebvre, L.-P., Banhart, J., Dunand, D. C. (2008). Porous metals and metallic foams: current status and recent developments. *Advanced Engineering Materials*, 10(9):775–787.
[4] Betts, C. (2012). Benefits of metal foams and developments in modelling techniques to assess their materials behaviour: a review. *Materials Science and Technology*, 28(2):129–143.
[5] Smith, B. H., Szyniszewski, S., Hajjar, J. F., Schafer, B. W., Arwade, S. R. (2012). Steel foam for structures: A review of applications, manufacturing and material properties. *Journal of Constructional Steel Research*, 71:1–10.
[6] Xia, X. C., Chen, X. W., Zhang, Z., Chen, X., Zhao, W. M., Liao, B., Hur, B. (2013). Effects of porosity and pore size on the compressive properties of closed-cell Mg alloy foam. *Journal of Magnesium and Alloys*, 1(4):330–335.
[7] Iijima, S. (1991). Helical microtubules of graphitic carbon. *Nature*, 354(6348):56–58.
[8] Liew, K., Lei, Z., Zhang, L. (2015). Mechanical analysis of functionally graded carbon nanotube reinforced composites: a review. *Composite Structures*, 120:90–97.
[9] Thanh, N. V., Khoa, N. D., Tuan, N. D., Tran, P., Duc, N. D. (2017). Nonlinear dynamic response and vibration of functionally graded carbon nanotube-reinforced composite (FG-CNTRC) shear deformable plates with temperature-dependent material properties and surrounded on elastic foundations. *Journal of Thermal Stresses*, 40(10):1254–1274.
[10] Mittal, G., Dhand, V., Rhee, K. Y., Park, S.-J., Lee, W. R. (2015). A review on carbon nanotubes and graphene as fillers in reinforced polymer nanocomposites. *Journal of Industrial and Engineering Chemistry*, 21:11–25.
[11] Papageorgiou, D. G., Kinloch, I. A., Young, R. J. (2017). Mechanical properties of graphene and graphene-based nanocomposites. *Progress in Materials Science*, 90:75–127.
[12] Rafiee, M. A., Rafiee, J., Wang, Z., Song, H., Yu, Z.-Z., Koratkar, N. (2009). Enhanced mechanical properties of nanocomposites at low graphene content. *ACS nano*, 3(12):3884–3890.
[13] Betts, C. (2012). Benefits of metal foams and developments in modelling techniques to assess their materials behaviour: a review. *Materials Science and Technology*, 28(2):129–143.
[14] Lefebvre, L.-P., Banhart, J., Dunand, D. C. (2008). Porous metals and metallic foams: current status and recent developments. *Advanced Engineering Materials*, 10(9):775–787.
[15] Wadley, H. N. G., Fleck, N. A., Evans, A. G. (2003). Fabrication and structural performance of periodic cellular metal sandwich structures. *Composites Science and Technology*, 63(16):2331–2343.
[16] Banhart, J. (2001). Manufacture, characterisation and application of cellular metals and metal foams. *Progress in Materials Science*, 46(6):559–632.
[17] Smith, B. H., Szyniszewski, S., Hajjar, J. F., Schafer, B. W., Arwade, S. R. (2012). Steel foam for structures: A review of applications, manufacturing and material properties. *Journal of Constructional Steel Research*, 71:1–10.
[18] Pompe, W., Worch, H., Epple, M., Friess, W., Gelinsky, M., Greil, P., Hempel, U., Scharnweber, D., Schulte, K. J. M. S. (2003). Functionally graded materials for biomedical applications. *Materials Science and Engineering: A*, 362(1-2):40–60.
[19] Phuong, N. T. B., Tu, T. M., Phuong, H. T., Van Long, N. (2019). Bending analysis of functionally graded beam with porosities resting on elastic foundation based on neutral surface position. *Journal of Science and Technology in Civil Engineering (STCE)-NUCE*, 13(1):33–45.
[20] Hangai, Y., Saito, K., Utsunomiya, T., Kitahara, S., Kuwazuru, O., Yoshikawa, N. (2013). Compression properties of Al/Al–Si–Cu alloy functionally graded aluminum foam fabricated by friction stir processing route. *Materials Transactions*, page M2012376.
[21] Hassani, A., Habibolahzadeh, A., Bafti, H. (2012). Production of graded aluminum foams via powder space holder technique. *Materials & Design*, 40:510–515.
[22] He, S.-Y., Zhang, Y., Dai, G., Jiang, J.-Q. (2014). Preparation of density-graded aluminum foam. *Materials Science and Engineering: A*, 618:496–499.
[23] Kitipornchai, S., Chen, D., Yang, J. (2017). Free vibration and elastic buckling of functionally graded porous beams reinforced by graphene platelets. *Materials & Design*, 116:656–665.
[24] Chen, D., Yang, J., Kitipornchai, S. (2017). Nonlinear vibration and postbuckling of functionally graded

graphene reinforced porous nanocomposite beams. *Composites Science and Technology*, 142:235–245.

[25] Yang, J., Chen, D., Kitipornchai, S. (2018). Buckling and free vibration analyses of functionally graded graphene reinforced porous nanocomposite plates based on Chebyshev-Ritz method. *Composite Structures*, 193:281–294.

[26] Li, K., Wu, D., Chen, X., Cheng, J., Liu, Z., Gao, W., Liu, M. (2018). Isogeometric analysis of functionally graded porous plates reinforced by graphene platelets. *Composite Structures*, 204:114–130.

[27] Endo, M., Kimura, N. (2007). An alternative formulation of the boundary value problem for the Timoshenko beam and Mindlin plate. *Journal of Sound and Vibration*, 301(1-2):355–373.

[28] Endo, M. (2015). Study on an alternative deformation concept for the Timoshenko beam and Mindlin plate models. *International Journal of Engineering Science*, 87:32–46.

[29] Senjanović, I., Vladimir, N., Tomić, M. (2013). An advanced theory of moderately thick plate vibrations. *Journal of Sound and Vibration*, 332(7):1868–1880.

[30] Senjanović, I., Vladimir, N., Hadžić, N. (2014). Modified Mindlin plate theory and shear locking-free finite element formulation. *Mechanics Research Communications*, 55:95–104.

[31] Nguyen, T. N., Ngo, T. D., Nguyen-Xuan, H. (2017). A novel three-variable shear deformation plate formulation: theory and Isogeometric implementation. *Computer Methods in Applied Mechanics and Engineering*, 326:376–401.

[32] Roberts, A. P., Garboczi, E. J. (2001). Elastic moduli of model random three-dimensional closed-cell cellular solids. *Acta Materialia*, 49(2):189–197.

[33] Mindlin, R. D. (1951). Influence of rotatory inertia and shear on flexural motions of isotropic, elastic plates. *Journal of Applied Mechanics*, 18:31–38.

[34] Reddy, J. N. (1984). A simple higher-order theory for laminated composite plates. *Journal of Applied Mechanics*, 51(4):745–752.

[35] Nguyen-Xuan, H., Thai, C. H., Nguyen-Thoi, T. (2013). Isogeometric finite element analysis of composite sandwich plates using a higher order shear deformation theory. *Composites Part B: Engineering*, 55:558–574.

[36] Thai, C. H., Kulasegaram, S., Tran, L. V., Nguyen-Xuan, H. (2014). Generalized shear deformation theory for functionally graded isotropic and sandwich plates based on isogeometric approach. *Computers & Structures*, 141:94–112.

[37] Baferani, A. H., Saidi, A. R., Jomehzadeh, E. (2011). An exact solution for free vibration of thin functionally graded rectangular plates. *Proceedings of the Institution of Mechanical Engineers, Part C: Journal of Mechanical Engineering Science*, 225(3):526–536.

[38] Yin, S., Hale, J. S., Yu, T., Bui, T. Q., Bordas, S. P. A. (2014). Isogeometric locking-free plate element: a simple first order shear deformation theory for functionally graded plates. *Composite Structures*, 118: 121–138.

[39] Yin, S., Yu, T., Liu, P. (2013). Free vibration analyses of FGM thin plates by isogeometric analysis based on classical plate theory and physical neutral surface. *Advances in Mechanical Engineering*, 5:634584.